Vietnam Journal of Mathematics (2018) 46: 967–985
https://doi.org/10.1007/s10013-018-0312-0

Shape Optimization for Interface Identification with Obstacle Problems

Björn Führ[1] · Volker Schulz[1] · Kathrin Welker[1]

Received: 21 December 2017 / Accepted: 7 August 2018 / Published online: 4 October 2018

Abstract
Shape optimization is an industrially highly relevant subject. Recently, it gained much interest due to novel developments in the usage of volumetric formulations of shape derivatives. This paper is based on recent results in the field of PDE constrained shape optimization and carries the achieved methodology over to shape optimization problems with constraints in the form of variational inequalities, in particular, in the form of obstacle problems. A novel expression for the volumetric shape derivative in this context is proven and numerical results of a descent strategy based on this expression are reported.

Keywords Shape optimization · Variational inequalities · Obstacle problem

Mathematics Subject Classification (2010) 65K15 · 49Q10 · 57N25

1 Introduction

The optimization of shapes is of high importance in a wide range of applications. As examples, we mention aerodynamic shape optimization [34], acoustic shape optimization [43], optimization of interfaces in transmission problems [11, 29, 31], shape optimization in thermo-elastic processes [42], inverse modeling of the skin structure [29], electrochemical machining [15] and image restoration and segmentation [16]. In an industrial context, often a priori parameterizations of the shapes of interest are used because of the resulting vector space framework matching standard optimization software. However, this limits the insight into the optimal shapes severely, because only shapes corresponding to the a priori parameterization can be reached. Thus, we focus here on shape optimization in the context of shape calculus, which does not suffer from this limitation.

This article is dedicated to the 70th birthday of Hans Georg Bock.

✉ Volker Schulz
volker.schulz@uni-trier.de

Kathrin Welker
welker@uni-trier.de

[1] Department of Mathematics, Trier University, FB IV, 54286 Trier, Germany

The subject of shape optimization is covered by several fundamental monographs [2, 8, 13, 25, 41]. So far, the focus of the research in shape optimization is on the theoretical framework, the study of existence of solutions and on the determination of shape derivatives. From a computational side of view, a differentiation tool which can automatically generate first and second order shape derivatives is recently presented in [33]. The optimization methodology is mostly limited to steepest descent methods based on the shape derivative with only very few exceptions [16, 32, 35, 37–39]. It is shown in [14] that a descent property is sufficient to give local convergence. However, only recently higher order optimization methods came into view, based on the interpretation of shape optimization as optimization on Riemannian shape manifolds in [35]. If one cannot work in vector spaces (as it is the case with shape optimization), Riemannian manifolds are the next best option. Optimization on finite dimensional manifolds is discussed in-depth in [1]. As shown in [24] and related papers, the set of $\mathcal{C}^\infty$-smooth shapes can be understood as Riemannian manifolds with tangent space defined by normal vector fields. As discussed in [35], the interpretation of tangent vectors as directional derivatives provides the bridge between the differential geometric concept of Riemannian shape manifolds and shape optimization. In [35], also a Riemannian shape Hessian is introduced, which is symmetric and provides a Taylor series expansion—in contrast to the classical notion of a shape Hessian, which is more precisely described as a second shape derivative. Furthermore, correlations between both Hessian concepts are discussed. This opens the door to optimization algorithms in the fashion of non-linear programming approaches. Based on this, the publication [38] presents a sequential quadratic programming (SQP) approach to shape optimization constrained by partial differential equations (PDEs) and demonstrates quadratic convergence. The major tool for the development of the respective Lagrange–Newton type methods is the concept of vector bundles associated with shape manifolds. The linear-quadratic subproblems in this approach are in the form of optimal control problems with boundary control of Neumann type.

The publications [37, 38] are only concerned with $\mathcal{C}^\infty$-smooth shapes, which limits the applicability to a certain extent. As a remedy, [39] suggests shape metrics of Steklov–Poincaré type, which also enable a unification of shape derivatives in Hadamard boundary form with equivalent shape derivatives in domain integral form. Based on these shape metrics, a novel shape space is proposed analogously to the construction in [24], but only with $H^{1/2}$-regularity of the shape boundary. This space of so-called $H^{1/2}$-shapes is investigated and redefined in [45] which enables its diffeological structure. In [10], it is shown for the case of star shaped domains that this regularity yields coercivity of the shape Hessian for a representative elliptic problem class. Furthermore, this novel approach enables the robust computation of optimal solutions for shape optimization problems, which can be classified as large deformations with respect to the initial shape and which involve non-differentiabilities, as illustrated in [36].

In this paper, we consider shape optimization problems which are constrained by variational inequalities (VIs), whose essential algorithmic ingredient is a semi-smooth Newton approach. In classical VIs, there is no explicit dependence on the domain, which adds an unavoidable source of non-linearity and non-convexity due to the non-linear and non-convex nature of shape spaces. So far, there are only very few approaches in the literature to this problem class. In [21], shape optimization of 2D elasto-plastic bodies is studied, where the shape is simplified to a graph. In [41, Chapter 4], shape derivatives for elliptic VI problems are presented in the form of solutions to VIs. In [26], shape optimization for 2D graph-like domains are investigated. Also [22, 23] present existence results for shape optimization problems which can be reformulated as optimal control problems, whereas [9, 12] show existence of solutions in a more general set-up. In [27, 28], level-set methods are proposed

and applied to graph-like two-dimensional problems. More recently, [15] presents a regularization approach to the computation of shape and topological derivatives in the context of elliptic VIs, thus circumventing the numerical problems in [41, Chapter 4].

This paper is organized as follows. In Section 2, besides a short review on the background of shape optimization, VI models are formulated. Furthermore, the corresponding shape derivative is given. Section 3 is concerned with the formulation of an optimization algorithm to solve VI constrained shape optimization problems. A key element of the optimization algorithm is the usage of linearized forward problems in order to reduce the computational effort required. This linearization idea follows the legacy of internal numerical differentiation due to Hans Georg Bock [5]. A numerical test framework and results are presented in Section 4.

2 Model Class

After setting up notation and terminology, we formulate the model problem and deduce its shape derivative.

2.1 Notations and Definitions

One focus in shape optimization is to investigate shape functionals. First, we define such a functional.

Definition 1 (Shape functional) Let D denote a non-empty subset of $\mathbb{R}^d$, where $d \in \mathbb{N}$. Moreover, $\mathcal{A} \subset \{\Omega \colon \Omega \subset D\}$ denotes a set of subsets. A function

$$J \colon \mathcal{A} \to \mathbb{R}, \quad \Omega \mapsto J(\Omega)$$

is called a shape functional.

In the following, let D be as in the definition above. Moreover, let $\{F_t\}_{t\in[0,T]}$ be a family of mappings $F_t \colon \overline{D} \to \mathbb{R}^d$ such that $F_0 = id$, where $T > 0$. This family transforms a domain $\Omega \subset D$ into *perturbed domains*

$$\Omega_t := F_t(\Omega) = \{F_t(x) \colon x \in \Omega\} \text{ with } \Omega_0 = \Omega$$

and the boundary $\Gamma = \partial\Omega$ into *perturbed boundaries*

$$\Gamma_t := F_t(\Gamma) = \{F_t(x) \colon x \in \Gamma\} \text{ with } \Gamma_0 = \Gamma.$$

Here, the family $\{F_t\}_{t\in[0,T]}$ is described by the perturbation of identity which is defined by $F_t(x) := x + tV(x)$ and used in the following.

This paper deals with VI constrained shape optimization problems, i.e.,

$$\min_{\Omega} J(\Omega),$$

where J is a shape functional additionally depends on a solution of a VI. To solve these problems, we need their shape derivatives. For the definition of shape derivatives or a detailed introduction into shape calculus, we refer to the monographs [8, 41]. In the following, the shape derivative of a shape functional J at Ω in direction of a sufficiently smooth vector field V is denoted by $DJ(\Omega)[V]$. Shape derivatives can always be expressed as

boundary integrals due to the Hadamard structure theorem [41, Theorem 2.27]. In many cases, the shape derivative arises in two equivalent notational forms:

$$DJ_\Omega[V] := \int_\Omega F(x)V(x)\,dx \qquad \text{(volume formulation)},$$
$$DJ_\Gamma[V] := \int_\Gamma f(s)V(s)^T n(s)\,ds \qquad \text{(surface formulation)}.$$

Here F is a (differential) operator acting linearly on the vector field V and $f \in L^1(\Gamma)$ with $DJ_\Omega[V] = DJ(\Omega)[V] = DJ_\Gamma[V]$.

In general, we have to deal with so-called material and shape derivatives of generic functions $p\colon \Omega \to \mathbb{R}$ in order to derive shape derivatives of objective shape functions depending on a solution of a VI. For their definitions and more details we refer to the literature, e.g., [30]. In the following, we denote the material derivative of p by $\dot{p}$ or $D_m(p)$ and the shape derivative of p in the direction of a vector field V is denoted by p'. The correlation between these two derivative concepts is

$$p' = \dot{p} - V^T \nabla p \quad \text{ in } \Omega.$$

In Section 2.2, the following rules for the material derivative are needed to derive shape derivatives of objective functions depending on solutions of VIs. For the material derivative the product rule holds, i.e.,

$$D_m(pq) = D_m pq + pD_m q. \tag{1}$$

While the shape derivative commutes with the gradient, the material derivative does not, but the following equality, which is proven in [4], holds:

$$D_m \nabla p = \nabla D_m p - \nabla V^T \nabla p. \tag{2}$$

The concept of material and shape derivatives of a function $p\colon \Omega \to \mathbb{R}$ can be extended to its boundary $\Gamma = \partial\Omega$. We mention only a few aspects. For more details we refer to the literature, e.g., [30]. Let $z\colon \Gamma \to \mathbb{R}$ be the trace on the boundary Γ of p. In this setting, the boundary shape derivative z' is defined by

$$z' = \dot{p} - V^T \nabla_\Gamma p.$$

In order to deduce shape derivative formulas we have to consider the derivative of perturbed objective functions, which are given by

$$\frac{d^+}{dt}\left(\int_{\Omega_t} p_t\,dx_t\right)\Big|_{t=0} = \int_\Omega \dot{p} + \operatorname{div}(V)p\,dx, \tag{3}$$
$$\frac{d^+}{dt}\left(\int_{\Gamma_t} z_t\,ds_t\right)\Big|_{t=0} = \int_\Gamma \dot{z} + \operatorname{div}_\Gamma(V)z\,ds, \tag{4}$$

where $\operatorname{div}_\Gamma(V)$ denotes the tangential divergence of V. For the proofs of (3)–(4) we refer to the literature, e.g., [13, 18, 44].

2.2 Problem Formulation and Shape Derivative

Let $\Omega \subset D$ be a bounded Lipschitz domain with boundary $\partial\Omega$, where D is as above. This domain is assumed to be partitioned in a subdomain $\Omega_{\text{out}} \subset \Omega$ and an interior domain $\Omega_{\text{int}} \subset \Omega$ with boundary $\Gamma_{\text{int}} := \partial\Omega_{\text{int}}$ such that $\Omega_{\text{out}} \sqcup \Omega_{\text{int}} \sqcup \Gamma_{\text{int}} = \Omega$, where $\sqcup$ denotes the disjoint union. We consider Ω depending on Γ_{int}. Figure 1 illustrates this situation. In the following, the boundary Γ_{int} of the interior domain is called the interface and an element

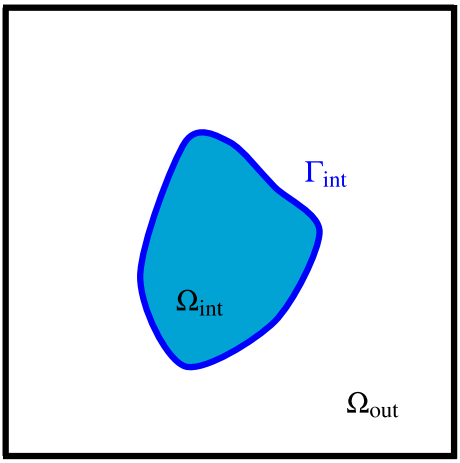

Fig. 1 Example of a domain $\Omega = \Omega_{\text{out}} \sqcup \Gamma_{\text{int}} \sqcup \Omega_{\text{int}}$

of an appropriate shape space (cf. Section 3.1). In contrast to the outer boundary $\partial\Omega$, which is assumed to be fixed, the inner boundary Γ_{int} is variable. The outer normal vector field to Ω_{int} is given by n.

Let $\nu > 0$ be an arbitrary constant and let $\lambda \in L^2(\Omega)$ be a function. For the objective function

$$J(y, \Omega) = j(y, \Omega) + j^{\text{reg}}(\Omega) \tag{5}$$

with

$$j(y, \Omega) := \frac{1}{2} \int_{\Omega} (y - \bar{y})^2 dx, \tag{6}$$

$$j^{\text{reg}}(\Omega) := \nu \int_{\Gamma_{\text{int}}} 1 ds \tag{7}$$

we consider the following VI constrained optimization problem in strong form:

$$\min_{\Gamma_{\text{int}}} J(y, \Omega) \tag{8}$$

subject to the following constraints:

$$-\triangle y + \lambda = f \quad \text{in } \Omega, \tag{9}$$

$$y \leq \psi \quad \text{in } \Omega, \tag{10}$$

$$\lambda \geq 0 \quad \text{in } \Omega, \tag{11}$$

$$\lambda(y - \psi) = 0 \quad \text{in } \Omega, \tag{12}$$

$$y = 0 \quad \text{on } \partial\Omega. \tag{13}$$

In (10), ψ denotes an obstacle and it is assumed $\psi \in H^4(\Omega)$ with $0 < \psi \leq M$ for some $M > 0$. We further assume

$$f = \begin{cases} f_{\text{int}} = \text{const.} & \text{in } \Omega_{\text{int}}, \\ f_{\text{out}} = \text{const.} & \text{in } \Omega_{\text{out}}. \end{cases} \tag{14}$$

Due to the jump in this coefficient, the formulation (9) is to be understood only formally. With the tracking-type objective j the model is fitted to data measurements $\bar{y}$. We assume $\bar{y} \in L^2(\Omega)$. The second term j^{reg} in the objective function J is a perimeter regularization. It is frequently used to overcome ill-posedness of optimization problems (cf. [3]). The VI

constituting the model equation above with $f_{\text{int}} = f_{\text{out}}$ is frequently used as a standard test object in theory and numerics for VI. It can be interpreted as a simplified version of the Signorini contact problem. The introduction of a piecewise constant source term, in order to construct a shape optimization problem, maybe physically interpreted as a piecewise constant load to be identified from deformation data. To the knowledge of the authors, this is the first attempt to this class of interface VI identification problems and the methodology can be generalized to similar and more complicated situations, which can be interpreted physically with more ease.

In general, the shape derivative of VI constrained shape optimization problems is not linear (cf. [15, 41]). This potential non-linearity of the shape derivative complicates its use in algorithms. In order to circumvent the problems related to the non-linearity, we consider the following regularized version of (8)–(13):

$$\min_{\Gamma_{\text{int}}} \; J(y_c, \Omega) \tag{15}$$

subject to

$$-\triangle y_c + \lambda_c = f \quad \text{in } \Omega, \tag{16}$$

$$y_c = 0 \quad \text{on } \partial\Omega \tag{17}$$

with

$$\lambda_c = \max(0, \overline{\lambda} + c(y_c - \psi))^2,$$

where $c > 0$ and $0 \leq \overline{\lambda} \in L^4(\Omega)$ fixed and ψ and f are as above. In [15], it is mentioned that for a large parameter c the associated solution of the regularized state (16)–(17) is an excellent approximation of the solution to the original VI (9)–(13). Moreover, it is shown in [15] that the shape derivative for the regularized problem converges to the solution of a linear problem which depends linearly on a perturbation vector field. Numerical tests in [15] show the efficiency of the approach to introduce a regularization of the VI, which allows to apply the usual theory for obtaining shape derivatives. Therefore, we consider (15)–(17) in the following.

The boundary value problem (16)–(17) admits a solution $y_c \in H_0^1(\Omega)$ (cf. [20]), which solves the weak formulation

$$a(y_c, p_c) = b(p_c) \quad \forall p_c \in H_0^1(\Omega),$$

where the bilinear form is given by

$$a(y_c, p_c) := \int_\Omega \nabla y_c^T \nabla p_c dx + \int_\Omega \lambda_c p_c dx - \int_{\Gamma_{\text{int}}} \left[\!\left[\frac{\partial y_c}{\partial n} p_c \right]\!\right] ds$$

and the linear form is defined by

$$b(p_c) := \int_\Omega f p_c dx.$$

The jump symbol $[\![\cdot]\!]$ denotes the discontinuity across the interface and is defined by

$$[\![\cdot]\!] \colon H_0^1(\Omega) \to H^{1/2}(\Gamma_{\text{int}}), \quad v \mapsto \text{tr}_1\left(v|_{\Omega_{\text{int}}}\right) - \text{tr}_2\left(v|_{\Omega_{\text{out}}}\right),$$

where $\text{tr}_1 \colon H_0^1(\Omega_{\text{int}}) \to H^{1/2}(\Gamma_{\text{int}})$ and $\text{tr}_2 \colon H_0^1(\Omega_{\text{out}}) \to H^{1/2}(\Gamma_{\text{int}})$ are the trace operator on the Sobolev spaces. We formulate explicitly the continuity of the state and the flux on the interface:

$$[\![y_c]\!] = 0, \quad \left[\!\left[\frac{\partial y_c}{\partial n} \right]\!\right] = 0 \quad \text{on } \Gamma_{\text{int}}. \tag{18}$$

The Lagrangian of

$$\min_{\Gamma_{\text{int}}} J(y_c, \Omega) \tag{19}$$

constrained by (16)–(17) is defined by

$$\mathfrak{L}(y_c, \Omega, p_c) = \mathfrak{L}_1(y_c, \Omega, p_c) + \mathfrak{L}_2(\Omega)$$

with

$$\begin{aligned} \mathfrak{L}_1(y_c, \Omega, p_c) &:= j(y_c, \Omega) + a(y_c, p_c) - b(p_c), \\ \mathfrak{L}_2(\Omega) &:= j^{\text{reg}}(\Omega) \end{aligned}$$

and $J = j + j^{\text{reg}}$ given in (5)–(7).

The adjoint problem to (19) constrained by (16)–(17), which we obtain from differentiating the Lagrangian $\mathfrak{L}$ with respect to y_c, is given in strong form by

$$-\triangle p_c + 2c\sqrt{\lambda_c} p = -(y_c - \bar{y}) \quad \text{in } \Omega, \tag{20}$$

$$p_c = 0 \quad \text{on } \partial\Omega \tag{21}$$

and the state equation to (19) constrained by (16)–(17), which we get by differentiating the Lagrangian $\mathfrak{L}$ with respect to p_c, is given in strong form by

$$-\triangle y_c + \lambda_c = f \quad \text{in } \Omega.$$

We formulate explicitly the interface condition to (20)–(21) as

$$[\![p_c]\!] = 0, \quad \left[\!\!\left[\frac{\partial p_c}{\partial n}\right]\!\!\right] = 0 \quad \text{on } \Gamma_{\text{int}}. \tag{22}$$

There are a lot of options to prove shape differentiability of shape functionals and to derive the shape derivative of constrained shape optimization problems, e.g., the min-max approach [8], the chain rule approach [41], the Lagrange method of Céa [6] and the rearrangement method [19]. In the sequel, we deduce the shape derivative of the shape functional j and j^{reg}. The sum of these two shape derivatives is the shape derivative of J. In this paper, we consider the Steklov–Poincaré metric and the optimization techniques established in [39]. These techniques and in particular the Steklov–Poincaré metric are rephrased in Section 3.1. Note that we need only the volume form of the shape derivative of j due to the Steklov–Poincaré metric. The existence of the shape derivative is given by the theorem of Correa and Seeger [7, Theorem 2.1]. The following theorem gives a representation of the shape derivative of j expressed as volume integral.

Theorem 1 *Let $y_c \in H^1(\Omega)$ denote the weak solution of (16)–(17). Moreover, $p_c \in H_0^1(\Omega)$ denotes the weak solution of the adjoint (20)–(21). Then the shape derivative of j in direction V is given by*

$$\begin{aligned} Dj(y_c, \Omega)[V] = \int_\Omega & -\nabla y_c^T \left(\nabla V + \nabla V^T\right) \nabla p_c - V^T \nabla f p_c - (y_c - \bar{y}) V^T \nabla \bar{y} \\ & + \operatorname{div}(V) \left(\frac{1}{2}(y_c - \bar{y})^2 + \nabla y_c^T \nabla p_c + \lambda_c p_c - f p_c\right) dx, \end{aligned} \tag{23}$$

where $\lambda_c = \max(0, \bar{\lambda} + c(y_c - \psi))^2$ with $c > 0$, $0 \leq \bar{\lambda} \in L^4(\Omega)$ and $\psi \in H^4(\Omega)$ with $0 < \psi \leq M$ for some $M > 0$.

Proof We consider the Lagrangian $\mathfrak{L}_1$. In analogy to [8, Chapter 10, Subsection 5.2], we can verify that

$$j(y_c, \Omega) = \min_{y_c \in H_0^1(\Omega)} \max_{p_c \in H_0^1(\Omega)} \mathfrak{L}_1(y_c, \Omega, p_c) \tag{24}$$

holds. We apply the theorem of Correa and Seeger on the right-hand side of (24). The verification of the assumptions of this theorem can be checked in the same way as in [8, Chapter 10, Subsection 6.4]. Applying the rules for differentiating volume and surface integrals given in (3)–(4) yields

$$\begin{aligned}
&D\mathfrak{L}_1(y_c, \Omega, p_c)[V] \\
&= \int_\Omega D_m\left(\frac{1}{2}(y_c - \bar{y})^2\right) + D_m\left(\nabla y_c^T \nabla p_c\right) + D_m\left(\lambda_c p_c\right) - D_m\left(f p_c\right) \\
&\quad + \operatorname{div}(V)\left(\frac{1}{2}(y_c - \bar{y})^2 + \nabla y_c^T \nabla p_c + \lambda_c p_c - f p_c\right) dx \\
&\quad - \int_{\Gamma_{\text{int}}} D_m\left(\left[\!\left[\frac{\partial y_c}{\partial n} p_c\right]\!\right]\right) + \operatorname{div}_{\Gamma_{\text{int}}}(V)\left[\!\left[\frac{\partial y_c}{\partial n} p_c\right]\!\right] ds,
\end{aligned}$$

where

$$D_m\left(\frac{1}{2}(y_c - \bar{y})^2\right) = (y_c - \bar{y}) D_m(y_c - \bar{y}) = (y_c - \bar{y})\dot{y_c} - (y_c - \bar{y}) V^T \nabla \bar{y}$$

the combination of (1) with (2) gives

$$D_m\left(\nabla y_c^T \nabla p_c\right) = \nabla \dot{y_c}^T \nabla p_c - \nabla y_c^T \left(\nabla V + \nabla V^T\right) \nabla p_c + \nabla y_c^T \nabla \dot{p_c},$$

the product rule (1) and the definition of λ_c leads to

$$D_m\left(\lambda_c p_c\right) = 2c\sqrt{\lambda_c}\, \dot{y_c} p_c + \lambda_c \dot{p_c}$$

and due to (1),

$$D_m(f p_c) = V^T \nabla f + f \dot{p_c}.$$

In summary, we obtain the following identity under consideration of the adjoint and design equation in weak form and by appropriate transformations:

$$\begin{aligned}
&D\mathfrak{L}_1(y_c, \Omega, p_c)[V] \\
&= \int_\Omega -\nabla y_c^T \left(\nabla V + \nabla V^T\right) \nabla p_c - V^T \nabla f p_c - (y_c - \bar{y}) V^T \nabla \bar{y} \\
&\quad + \operatorname{div}(V)\left(\frac{1}{2}(y_c - \bar{y})^2 + \nabla y_c^T \nabla p_c + \lambda_c p_c - f p_c\right) dx \\
&\quad - \int_{\Gamma_{\text{int}}} \left[\!\left[D_m\left(\frac{\partial y_c}{\partial n}\right) p_c\right]\!\right] + \left[\!\left[\frac{\partial y_c}{\partial n} \dot{p_c}\right]\!\right] + \operatorname{div}_{\Gamma_{\text{int}}}(V)\left[\!\left[\frac{\partial y_c}{\partial n} p_c\right]\!\right] ds.
\end{aligned}$$

Let ϕ and ψ be two functions with

$$\phi := \begin{cases} \phi_{\text{out}} & \text{in } \Omega_{\text{out}}, \\ \phi_{\text{int}} & \text{in } \Omega_{\text{int}}, \end{cases} \qquad \psi := \begin{cases} \psi_{\text{out}} & \text{in } \Omega_{\text{out}}, \\ \psi_{\text{int}} & \text{in } \Omega_{\text{int}}. \end{cases}$$

Due to the identity $[\![\Phi\Psi]\!] = [\![\Phi]\!]\Psi_{\text{out}} + \Phi_{\text{int}}[\![\Psi]\!] = \Phi_{\text{out}}[\![\Psi]\!] + [\![\Phi]\!]\Psi_{\text{int}}$, which implies

$$[\![\Phi\Psi]\!] = 0 \quad \text{if} \quad [\![\Phi]\!] = 0 \wedge [\![\Psi]\!] = 0,$$

and the interface conditions (18) and (22), the above interface integral vanishes. By applying the theorem of Correa and Seeger, we obtain (23). □

The objective function J includes the perimeter regularization term j^{reg}. We get the shape derivative of this regularization term by applying (4):

$$Dj^{\mathrm{reg}}(\Omega)[V] = \nu \int_{\Gamma_{\mathrm{int}}} \mathrm{div}_{\Gamma_{\mathrm{int}}}(V) ds,$$

i.e.,

$$\boxed{Dj^{\mathrm{reg}}(\Omega)[V] = \nu \int_{\Gamma_{\mathrm{int}}} \mathrm{div}(V) - \langle V, n\rangle n ds.} \tag{25}$$

Remark 1 In the literature, for the shape derivative of a perimeter regularization, the formulation

$$Dj^{\mathrm{reg}}(\Omega)[V] = \nu \int_{\Gamma_{\mathrm{int}}} \kappa \, \langle V, n\rangle \, ds \qquad (\kappa := \mathrm{div}_{\Gamma_{\mathrm{int}}}(n) \text{ mean curvature of } \Gamma_{\mathrm{int}})$$

is much more known instead of (25). However, as outlined in [40], formulation (25) is attractive from a computational point of view, since the evaluation of κ in each iteration is a surface-only operation.

So far, we have deduced derivatives. However, in order to optimize on shape spaces, we need the gradients with respect to the inner product under consideration. In the next section, we consider the Steklov–Poincaré metric.

3 Algorithm for VI Constrained Shape Optimization Problems

This section summarizes the way from shape derivatives to an entire algorithm to solve VI constrained shape optimization problems in a suitable shape space.

3.1 Optimization Based on Steklov–Poincaré Metrics

Shape optimization problems can be embedded in the framework of optimization on shape spaces as outlined, e.g., in [35, 44]. In general, finding a shape space and an associated metric is a challenging task and different approaches lead to various models. There exists no common shape space or shape metric suitable for all applications. The specific situation is essential for the suitability of a certain approach. In the setting of VI constrained shape optimization, one has to deal with polygonal shape representations from a computational point of view. This is because finite element (FE) methods are usually used to discretize the models. In [39], a shape space which is suitable, e.g., for the application of FE methods, is proposed. This space of so-called $H^{1/2}$-shapes is investigated and redefined in [45] which enables its diffeological structure. In the following, we consider space of $H^{1/2}$-shapes together with the Steklov–Poincaré metric in order to formulate optimization methods to solve VI constrained shape optimization problems.

In our setting, we think of shapes as boundary contours of deformed objects. We consider so-called (d-dimensional) *Lipschitz shapes* Γ_0 which are defined as the boundaries $\Gamma_0 = \partial\mathcal{X}_0$ of compact Lipschitz domains $\mathcal{X}_0 \subset \mathbb{R}^d$ with $\mathcal{X}_0 \neq \emptyset$. Shapes arise from H^1-deformations of such Lipschitz sets $\mathcal{X}_0$. These H^1-deformations, evaluated at a Lipschitz shape Γ_0, give deformed shapes Γ if the deformations are injective and continuous. These shapes are called of class $H^{1/2}$. The set of all these shapes is defined as follows:

Definition 2 (Shape space $\mathcal{B}^{1/2}$) Let $\Gamma_0 \subset \mathbb{R}^d$ be a d-dimensional Lipschitz shape. The space of all d-dimensional $H^{1/2}$-shapes is given by

$$\mathcal{B}^{1/2}(\Gamma_0, \mathbb{R}^d) := \mathcal{H}^{1/2}(\Gamma_0, \mathbb{R}^d)/\sim,$$

where

$$\mathcal{H}^{1/2}(\Gamma_0, \mathbb{R}^d) := \{w\colon w \in H^{1/2}(\Gamma_0, \mathbb{R}^d) \text{ injective, continuous; } w(\Gamma_0) \text{ Lipschitz shape}\} \tag{26}$$

and the equivalence relation $\sim$ is given by

$$w_1 \sim w_2 \Leftrightarrow w_1(\Gamma_0) = w_2(\Gamma_0), \text{ where } w_1, w_2 \in \mathcal{H}^{1/2}(\Gamma_0, \mathbb{R}^d).$$

If $\Gamma \in \mathcal{B}^{1/2}(\Gamma_0, \mathbb{R}^d)$ is smooth enough to admit a normal vector field n, the following isomorphism arises from definition (26):

$$T_\Gamma \mathcal{B}^{1/2}(\Gamma_0, \mathbb{R}^d) \cong \{\phi\colon \phi \in H^{1/2}(\Gamma) \text{ continuous}\}. \tag{27}$$

We consider the following scalar products, the so-called *Steklov–Poincaré metrics* (cf. [39]):

$$g^S\colon H^{1/2}(\Gamma_{\text{int}}) \times H^{1/2}(\Gamma_{\text{int}}) \to \mathbb{R},$$
$$(\alpha, \beta) \mapsto \langle \alpha, (S^{pr})^{-1}\beta\rangle = \int_{\Gamma_{\text{int}}} \alpha(s) \cdot [(S^{pr})^{-1}\beta](s)\, ds.$$

Here S^{pr} denotes the projected Poincaré–Steklov operator which is given by

$$S^{pr}\colon H^{-1/2}(\Gamma) \to H^{1/2}(\Gamma), \quad \alpha \mapsto (\gamma_0 U)^T n,$$

where $\gamma_0\colon H_0^1(\Omega, \mathbb{R}^d) \to H^{1/2}(\Gamma, \mathbb{R}^d)$, $U \mapsto U|_\Gamma$ and $U \in H_0^1(\Omega, \mathbb{R}^d)$ solves the Neumann problem

$$a(U, V) = \int_\Gamma \alpha \cdot (\gamma_0 V)^T n\, ds \quad \forall V \in H_0^1(\Omega, \mathbb{R}^d)$$

with a being a symmetric and coercive bilinearform.

We are now able to formulate an optimization algorithm on the shape space $\mathcal{B}^{1/2}(\Gamma_0, \mathbb{R}^d)$ with respect to g^S. Before we can do that, we have to state its connection to shape calculus. Due to the Hadamard structure theorem, there exists a scalar distribution r on the boundary of the domain under consideration. If we assume $r \in L^1(\Gamma)$ and $V|_\Gamma = \alpha n$, the shape derivative can be expressed as the boundary integral

$$DJ_\Gamma[V] = \int_\Gamma \alpha r\, ds. \tag{28}$$

Due to the isomorphism (27) and the expression (28), we can state the connection of $\mathcal{B}^{1/2}(\Gamma_0, \mathbb{R}^d)$ with respect to the Steklov–Poincaré metric g^S to shape calculus. The distribution r is often called the *shape gradient*. This is confusing, because one has to note that gradients always depend on chosen scalar products defined on the space under consideration. It rather means that r is the usual L^2-shape gradient. However, we have to find a representation of the shape gradient with respect to g^S. Such a representation $h \in T_\Gamma \mathcal{B}^{1/2}(\Gamma_0, \mathbb{R}^d) \cong \{h\colon h \in H^{1/2}(\Gamma) \text{ continuous}\}$ is determined by

$$g^S(\phi, h) = (r, \phi)_{L^2(\Gamma)}, \tag{29}$$

which is equivalent to

$$\int_\Gamma \phi(s) \cdot [(S^{pr})^{-1}h](s)\, ds = \int_\Gamma r(s)\phi(s)\, ds \tag{30}$$

for all continuous $\phi \in H^{1/2}(\Gamma)$. Based on the connection (29) we can formulate an algorithm to solve VI constrained shape optimization problems on $\mathcal{B}^{1/2}(\Gamma_0, \mathbb{R}^d)$ with respect to g^S. From (30) we get $h = S^{pr} r = (\gamma_0 U)^T n$, where $U \in H_0^1(\Omega, \mathbb{R}^d)$ solves

$$a(U, V) = \int_\Gamma r \cdot (\gamma_0 V)^T n \, ds = DJ_\Gamma[V] = DJ_\Omega[V] \quad \forall V \in H_0^1(\Omega, \mathbb{R}^d).$$

This means that we get the gradient representation h and the mesh deformation U all at once and that we have to solve

$$a(U, V) = b(V) \tag{31}$$

for all test functions $V \in H_0^1(\Omega, \mathbb{R}^d)$ in the optimization algorithm, where b is a linear form and given by

$$b(V) := DJ_{\text{vol}}(\Omega)[V] + DJ_{\text{surf}}(\Omega)[V].$$

Here $J_{\text{surf}}(\Omega)$ denotes parts of the objective function leading to surface shape derivative expressions—in our setting above, the perimeter regularization j^{reg}. The shape derivative $DJ_{\text{surf}}(\Omega)[V]$ of these terms are incorporated as Neumann boundary conditions. Parts of the objective function leading to volume shape derivative expressions are denoted by $J_{\text{vol}}(\Omega)$—in our setting above, the objective function j. However, note that from a theoretical point of view the volume and surface shape derivative formulations have to be equal to each other for all test functions. Thus, $DJ_{\text{vol}}[V]$ is assembled only for test functions V whose support includes Γ, i.e.,

$$DJ_{\text{vol}}(\Omega)[V] = 0 \quad \forall V \text{ with } \text{supp}(V) \cap \Gamma = \emptyset.$$

We call (31) the *deformation equation*. The entire optimization algorithm is given in Fig. 2 and explained in detail in the next subsection.

Remark 2 An unmodified right-hand side of the deformation equation (31) leads to wrong meshes due to discretization errors. This is outlined and illustrated in [39].

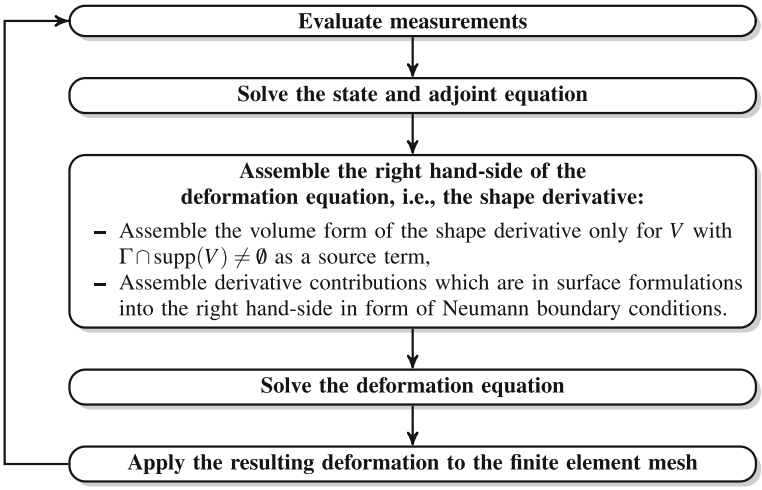

Fig. 2 Optimization algorithm based on the Steklov–Poincaré metric

3.2 Algorithmic Details

In this subsection, we consider the optimization algorithm given in Fig. 2 in details for our model problem. In particular, we explain how the state equation can be solved and how the deformation equation looks like.

3.2.1 Linearized Modified Primal-Dual Active Set Algorithm

In the optimization algorithm based on the Steklov–Poincaré metric (cf. Fig. 2), we have to solve the state equation (9)–(13). In the following, we concentrate on its regularized version given in (16)–17. To solve this problem, we adapt the primal-dual active set (PDAS) algorithm given in [17], where a similar regularized problem is solved. The solution of the problem described in [17] and the solution of our model problem converge to the same result (cf. [15]). In Algorithm 1, the PDAS algorithm of [17] is adapted to our problem.

Algorithm 1 Modified PDAS (mPDAS) algorithm

(1) Choose y_0, $k = 0$ and $\lambda_0 = 0$.

(2) $\mathcal{A}_{k+1} := \{x : \ [\lambda_k + c(y - \psi)](x) > 0\}$ and $\mathcal{I}_{k+1} := \Omega \backslash \mathcal{A}_{k+1}$.

(3) Compute $y_{k+1} \in H_0^1(\Omega)$ as solution of

$$a(y_{k+1}, v) + \left(\left[\lambda_k + c(y_{k+1} - \psi) \right]^2, \chi_{\mathcal{A}_{k+1}} v \right) = (f, v) \qquad \forall v \in H_0^1(\Omega). \tag{32}$$

(4) $\lambda_{k+1} := \begin{cases} 0 & \text{if } x \in \mathcal{I}_{k+1}, \\ \lambda_k + c(y_{k+1} - \psi) & \text{if } x \in \mathcal{A}_{k+1}. \end{cases}$

(5) Stop or $k := k + 1$ and go to (2).

Note that Algorithm 1 involves a non-linear equation (equation (32) is not linear in y_{k+1}). In order to avoid solving a non-linear equation, we compute the increment $\Delta y := y_{k+1} - y_k$ instead y_{k+1}, i.e., the new iterate is given by $y_{k+1} = y_k + \Delta y$. Computing Δy instead of y_{k+1} leads to the following equation:

$$a(y_k + \Delta y, v) + \left([\lambda_k + c(y_k + \Delta y - \psi)]^2, \chi_{\mathcal{A}_{k+1}} v \right) = (f, v) \qquad \forall v \in H_0^1(\Omega). \tag{33}$$

The second term in (33) is still non-linear due to the square, but it is possible to linearize this equation. By putting the linearization

$$(\lambda_k + c(y_k + \Delta y - \psi))^2 \doteq (\lambda_k + c(y_k - \psi))^2 + 2c\Delta y(\lambda_k + c(y_k - \psi))$$

in (33), we get

$$\begin{aligned} &a(\Delta y, v) + (2c\Delta y \, [\lambda_k + c(y_k - \psi)], \chi_{\mathcal{A}_{k+1}} v) \\ &= (f, v) - a(y_k, v) - \left([\lambda_k + c(y_k - \psi)]^2, \chi_{\mathcal{A}_{k+1}} v \right) \qquad \forall v \in H_0^1(\Omega), \end{aligned} \tag{34}$$

which is linear in Δy. The idea of this linearization is inspired by the concept of internal numerical differentiation, which is due to Hans Georg Bock [5] and his legacy. Due to linearized version (34) of (32), we can formulate the linearized mPDAS algorithm

(cf. Algorithm 2). Here the third step can be iterated several times. This should be done as soon as y_{k+1} changes significantly.

Algorithm 2 Linearized mPDAS (lmPDAS) algorithm

(1) Choose y_0, $k = 0$ and $\lambda_0 = 0$.

(2) $\mathcal{A}_{k+1} := \{x : [\lambda_k + c(y - \psi)](x) > 0\}$ and $\mathcal{I}_{k+1} := \Omega \backslash \mathcal{A}_{k+1}$.

(3) (i) Compute Δy as solution of

$$\begin{aligned} &a(\Delta y, v) + \left(2c\Delta y\,[\lambda_k + c(y_k - \psi)]\,, \chi_{\mathcal{A}_{k+1}} v\right) \\ &= (f, v) - a(y_k, v) - \left([\lambda_k + c(y_k - \psi)]^2\,, \chi_{\mathcal{A}_{k+1}} v\right) \qquad \forall v \in H_0^1(\Omega). \end{aligned}$$

(ii) $y_{k+1} := y_k + \Delta y$.

(4) $\lambda_{k+1} := \begin{cases} 0 & \text{if } x \in \mathcal{I}_{k+1}, \\ \lambda_k + c(y_{k+1} - \psi) & \text{if } x \in \mathcal{A}_{k+1}. \end{cases}$

(5) Stop or $k := k + 1$ and go to (2).

3.2.2 Deformation Equation

An essential part of the shape optimization techniques outlined in Fig. 2 is to update the FE mesh after each iteration. For this purpose, we use a solution of the deformation equation (31). The right-hand side of this equation is given by the shape derivative and the left-hand side can be given for example by the linear elasticity equation. If we choose the linear elasticity equation as left-hand side, the deformation equation—for the model problem above—is given by

$$\int_\Omega \sigma(U) : \epsilon(V)\, dx = Dj(y_c, \Omega)[V] + Dj^{\text{reg}}(\Omega)[V] \quad \forall V \in H_0^1(\Omega, \mathbb{R}^2), \tag{35}$$

where $\sigma(U) := \lambda \text{Tr}(\epsilon(U))I + 2\mu\epsilon(U)$ and $\epsilon(U) := \frac{1}{2}(\nabla U + \nabla U^T)$ are the strain and stress tensor, respectively, and $Dj(y_c, \Omega)[V]$ given in (23) and $Dj^{\text{reg}}(\Omega)[V]$ given in (25) are the shape derivative of the tracking-type objective functional (6) and the regularization term (7), respectively. Recall that the volume shape derivative expression $Dj(y_c, \Omega)[V]$ is only assembled for all test functions V whose support includes Γ_{int} in order to avoid wrong mesh deformations due to discretization errors (cf. Section 3.1). Here λ and μ denote the Lamé parameters, which can be expressed in terms of Young's modulus E and Poisson's ratio ν as

$$\lambda = \frac{\nu E}{(1+\nu)(1-2\nu)}, \quad \mu = \frac{E}{2(1+\nu)}.$$

The solution $U : \Omega \to \mathbb{R}^2$ of (35) is added to the coordinates of the FE nodes. The Lamé parameters do not need to have a physical meaning here. It is rather essential to understand their effect on the mesh deformation. Here E states the stiffness of the material, which enables to control the step size for the shape update, and λ gives the ratio how much the mesh expands in the remaining coordinate directions when compressed in one particular direction. The Lamé parameters should not be chosen constant. In [36], it is observed that locally varying Lamé parameters have a good influence on the mesh. E.g., a good strategy

is to choose $\lambda = 0$ and μ as the solution of the following Laplace equation:

$$\begin{aligned} -\Delta\mu &= 0 \qquad \text{in } \Omega, \\ \mu &= \mu_{\max} \quad \text{on } \Gamma_{\text{int}}, \\ \mu &= \mu_{\min} \quad \text{on } \partial\Omega. \end{aligned} \tag{36}$$

Here $\mu_{\min},\ \mu_{\max} \in \mathbb{R}$ influence the step size of the optimization algorithm. A small step is achieved by the choice of a large $\mu_{\max}$.

3.2.3 Summary

In consideration of Algorithm 2 and the discussion about the deformation equation, we can formulate a technique to solve our model problem. Such an technique is outlined in Fig. 3. In the next section, we apply this technique and give the corresponding numerical results.

4 Numerical Results

We implement Algorithm 3 in Python together with the library FEniCS. In this section, the results of this method are analyzed for two numerical experiments, the deformation of an ellipse into a circle and the moving and magnification of a circle.

The weak forms of the PDE models involved are discretized using standard linear finite elements. We use test cases within the domain $\Omega = (0, 1)^2$, which contains a compact and closed subset Ω_{int} with variable boundary Γ_{int} (cf. Fig. 1). The parameter f_{int} is valid in the interior Ω_{int} and chosen as $f_{\text{int}} = 100$, and the parameter f_{ext} is valid in the exterior $\Omega_{\text{ext}} = \Omega \backslash \overline{\Omega}_{\text{int}}$ and chosen as $f_{\text{ext}} = -10$. Further, the perimeter regularization in (5) is weighted by $\nu = 0.01$.

The constant c in the regularized version (16)–(17) of (9)–(13) is given by $c = 5$. Figure 4c visualizes the corresponding λ_5 in (16)–(17), where the obstacle is chosen as

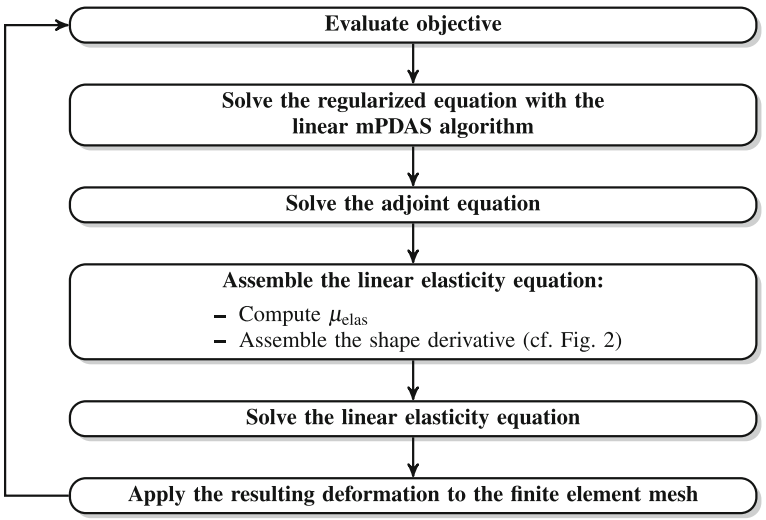

Fig. 3 Optimization algorithm to solve the model problem

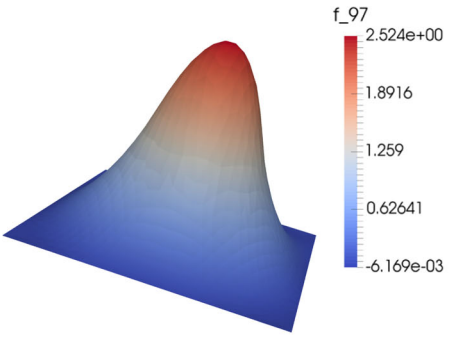

(a) Solution of the regularized state equation without obstacle

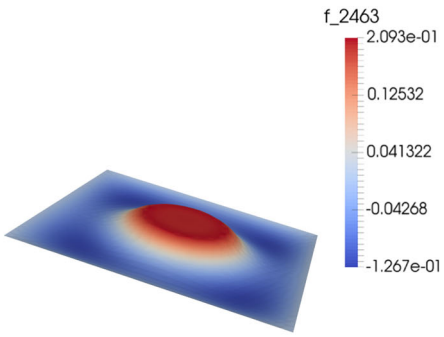

(b) Solution of the regularized state equation with $\psi = 0.2$

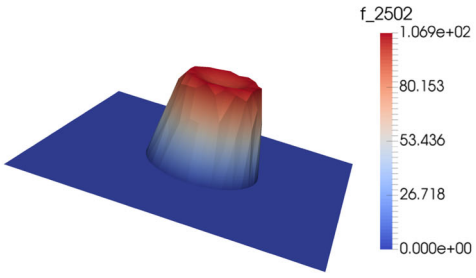

(c) Corresponding λ_5

Fig. 4 Solution of the regularized state equation with $c = 5$ and without and with obstacle $\psi = 0.2$ and the corresponding λ_5

$\psi = 0.2$. Moreover, Fig. 4 illustrates the solution of the regularized state equation without obstacle (Fig. 4a) and with obstacle $\psi = 0.2$ (Fig. 4b). In the following two numerical experiments, we choose different obstacles in order to decode its influence on the optimization method and stop the iteration process if the shape derivative value is smaller than 0.001. We observed that we need more iterations for tighter obstacles, i.e., small values for ψ.

In order to update the FE mesh after each iteration, we use the solution of the deformation equation, which is chosen in our experiments by (35). The solution $U : \Omega \to \mathbb{R}^2$ is then added to the coordinates of the FE nodes. We choose the Lamé parameters in (35) as described in Section 3.2.2, i.e., $\lambda = 0$ and μ as solution of the Poisson equation (36), where we set $\mu_{\min} = 1$ and $\mu_{\max} = 20$.

4.1 Ellipse to Circle

In the first numerical experiment, an ellipse is deformed into a centered circle with radius $r = 0.2$. We build artificial data $\bar{y}$ by solving the state equation for the setting $\overline{\Omega}_{\text{int}} := \{(x, y) \in (0, 1)^2 : (x-0.5)^2 + (y-0.5)^2 < 0.2^2\}$. Then, we add noise to the measurements $\bar{y}$, which is distributed according to $\mathcal{N}(0.0, 0.5)$. Afterwards, we choose the initial domain by $\Omega_{\text{int}} := \{(x, y) \in (0, 1)^2 : \frac{(x-0.5)^2}{0.15^2} + \frac{(y-0.5)^2}{0.25^2} < 1\}$. Figure 7a illustrates the interior boundary Γ_{int} around the initial domain Ω_{int} and the disturbed target domain $\overline{\Omega}_{\text{int}}$ in red color. The shapes between the initial and target shapes are the shape iterates.

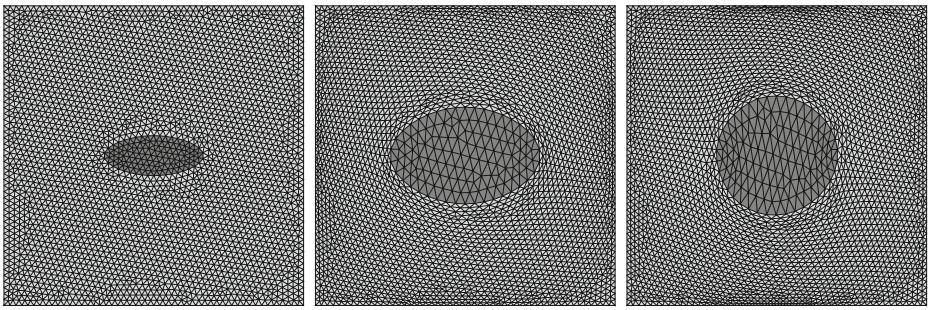

Fig. 5 First test case. The ellipse is deformed into a circle after 396 iterations

We performed computations on an unstructured grid with about 1 500 elements and on an uniformly refined grid with about 6 000 triangles. In Fig. 5, the left picture shows the initial shape geometry and the corresponding finest mesh and the right picture illustrates the final shape together with the deformed mesh. In this test run, the final shape is achieved after 396 iterations. The shape geometry after 14 iterations with the deformation of the mesh are illustrated in the middle picture of Fig. 5. This figure shows two behaviors:

- The largest deformations are at the beginning of the iteration process. This affects the values of the objective functional and the right-hand side of the deformation equation (35), i.e., the shape derivative. The values decrease very rapidly at the beginning. Afterwards, the values level off and remain at a similar level.
- In the interior domain, the elements are magnified by the mesh deformations. In order to avoid this, e.g., we can choose locally adapted meshes. Another possibility is to re-mesh after a few iterations which would allow us to operate on coarse meshes.

4.2 Moving and Magnification of a Circle

In the second experiment, we focus on the moving and magnification of a small centered circle with radius $r = 0.2$. The initial domain is given by $\Omega_{\text{int}} := \{(x, y) \in (0, 1)^2 \colon (x - 0.5)^2 + (y - 0.5)^2 < 0.2^2\}$. The data $\bar{y}$ is built by solving the state equation for the setting $\overline{\Omega}_{\text{int}} := \{(x, y) \in (0, 1)^2 \colon (x - 0.45)^2 + (y - 0.45)^2 < 0.25^2\}$. These measurements $\bar{y}$ are disturbed by adding noise to $\bar{y}$, which is distributed according to $\mathcal{N}(0.0, 0.5)$. In Fig. 7b, the interior boundary Γ_{int} around the initial domain Ω_{int} and the disturbed target domain

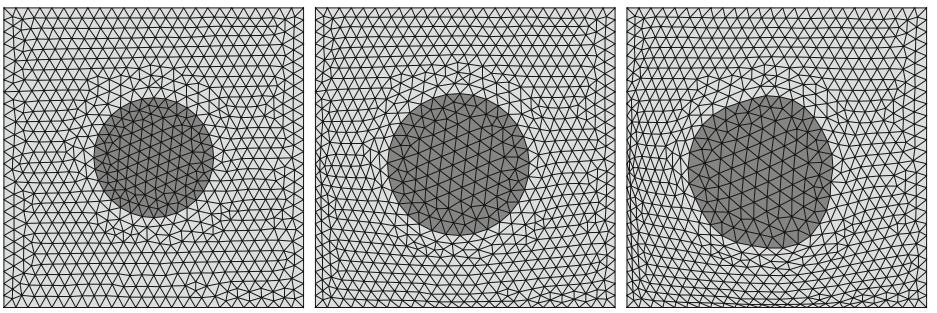

Fig. 6 Second test case. The circle is moved and magnified after 523 iterations

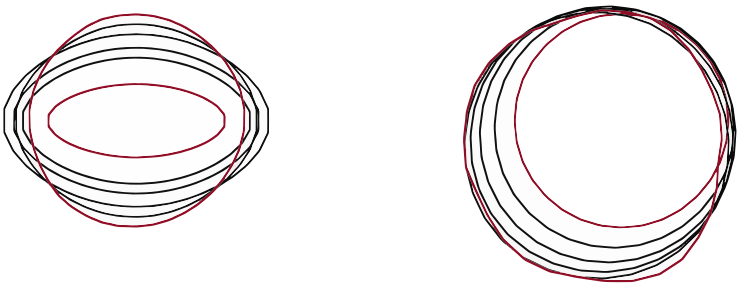

(a) First test case: An ellipse is deformed to a circle

(b) Second test case: A circle is moved and magnified

Fig. 7 Shape deformations. The initial and final shapes are colored in red

$\overline{\Omega}_{\text{int}}$ are visualized in red color. The shapes between these two are the shape iterates and show how the target shapes arises out of the initial shape.

As in the first experiment, we performed computations on two grids: A coarse one with about 1 500 elements and a much finer grid with about 6 000 triangles. Figure 6 shows the initial (left picture) and the final shape geometry (right picture) together with their corresponding finest meshes. The final shape is achieved after 523 iterations in this test run. Moreover, in the middle picture of Fig. 6, the shape geometry after 4 iterations with the finest mesh is illustrated. As already observed in the first experiment, the largest deformations are at the beginning of the iteration process as one can clearly see in Fig. 6. The area, where the measurements are generated, is achieved very early in the optimization process. This has influences on the values of the objective functional. In the beginning, the objective functional decreases very largely and levels off after about 25 iterations. Afterwards, the objective values remains at a similar level. The values of the assembled right-hand side of the deformation equation (35), i.e., the shape derivative, also shows such a behavior. In contrast to the first example, we do not observe that the elements of the interior domain are magnified by the mesh deformations (Fig. 7).

5 Conclusion

This paper gives a novel theoretical result on volumetric shape derivatives for shape optimization problems with constraints in the form of variational inequalities, in particular, in the form of obstacle problems. This derivative is used within the shape optimization framework established in [39] based on Steklov–Poincaré type shape metrics. A key element of the optimization algorithm is the usage of linearized forward problems in order to reduce the computational effort required. This linearization idea follows the legacy of internal numerical differentiation due to Hans Georg Bock [5]. We show that the resulting methodology is effective. Further, it is observed that the algorithmic performance deteriorates, if the obstacle problem is strongly binding, i.e., if the active region is large. This aspect will be discussed in more detail in subsequent papers.

Acknowledgements This work has been supported by the German Research Foundation within the priority program SPP 1962 Non-smooth and Complementarity-based Distributed Parameter Systems: Simulation and Hierarchical Optimization under contract number Schu804/15-1 and the research training group 2126 Algorithmic Optimization.

References

1. Absil, P.-A., Mahony, R., Sepulchre, R.: Optimization Algorithms on Matrix Manifolds. Princeton University Press, Princeton (2008)
2. Allaire, G.: Conception Optimale de Structures. Mathématiques & Applications, vol. 58. Springer, Berlin (2007)
3. Ameur, H.B., Burger, M., Hackl, B.: Level set methods for geometric inverse problems in linear elasticity. Inverse Probl. **20**, 673–696 (2004)
4. Berggren, M.: A unified discrete–continuous sensitivity analysis method for shape optimization. In: Fitzgibbon, W. et al. (eds.) Applied and Numerical Partial Differential Equations. Computational Methods in Applied Sciences, vol. 15, pp. 25–39. Springer, Dordrecht (2010)
5. Bock, H.G.: Numerical treatment of inverse problems in chemical reaction kinetics. In: Ebert, K.H., Deuflhard, P., Jäger, W. (eds.) Modelling of Chemical Reaction Systems. Springer Series in Chemical Physics, vol. 18, pp. 102–125. Springer, Berlin (1981)
6. Céa, J.: Conception optimale ou identification de formes calcul rapide de la dérivée directionelle de la fonction coût. RAIRO Model Math. Anal. Numér. **20**, 371–402 (1986)
7. Correa, R., Seeger, A.: Directional derivative of a minimax function. Nonlinear Anal. **9**, 13–22 (1985)
8. Delfour, M.C., Zolésio, J.P.: Shapes and Geometries: Analysis, Differential Calculus, and Optimization. SIAM, Philadelphia (2001)
9. Denkowski, Z., Migorski, S.: Optimal shape design for hemivariational inequalities. Univ. Iagell. Acta Mat. **36**, 81–88 (1998)
10. Eppler, K., Harbrecht, H., Schneider, R.: On convergence in elliptic shape optimization. SIAM J. Control Optim. **46**, 61–83 (2007)
11. Gangl, P., Laurain, A., Meftahi, H., Sturm, K.: Shape optimization of an electric motor subject to nonlinear magnetostatics. arXiv:1501.04752 (2015)
12. Gasiński, L.: Mapping method in optimal shape design problems governed by hemivariational inequalities. In: Cagnol, J., Polis, M.P., Zolésio, J. (eds.) Shape Optimization and Optimal Design. Lecture Notes in Pure and Applied Mathematics, vol. 216, pp. 277–288. Marcel Dekker, New York (2001)
13. Haslinger, J., Mäkinen, R.A.E.: Introduction to Shape Optimization: Theory, Approximation, and Computation. Advances in Design and Control. SIAM, Philadelphia (2003)
14. Hintermüller, M.: Fast level set based algorithms using shape and topological sensitivity information. Control Cybern. **34**, 305–324 (2005)
15. Hintermüller, M., Laurain, A.: Optimal shape design subject to elliptic variational inequalities. SIAM J. Control Optim. **49**, 1015–1047 (2011)
16. Hintermüller, M., Ring, W.: A second order shape optimization approach for image segmentation. SIAM J. Appl. Math. **64**, 442–467 (2003)
17. Ito, K., Kunisch, K.: Semi-smooth Newton methods for variational inequalities of the first kind. ESAIM: Math. Model. Numer. Anal. **37**, 41–62 (2003)
18. Ito, K., Kunisch, K.: Lagrange Multiplier Approach to Variational Problems and Applications. Advances in Design and Control, vol. 15. SIAM, Philadelphia (2008)
19. Ito, K., Kunisch, K., Peichl, G.H.: Variational approach to shape derivatives. ESAIM: Control Optim. Calc. Var. **14**, 517–539 (2008)
20. Kinderlehrer, D., Stampacchia, G.: An Introduction to Variational Inequalities and Their Applications. Classics in Applied Mathematics, vol. 31. SIAM, Philadelphia (2000)
21. Kočvara, M., Outrata, J.V.: Shape optimization of elasto-plastic bodies governed by variational inequalities. In: Zolésio, J. (ed.) Boundary Control and Variation. Lecture Notes in Pure and Applied Mathematics, vol. 163, pp. 261–271. Marcel Dekker, New York (1994)
22. Liu, W.B., Rubio, J.E.: Optimal shape design for systems governed by variational inequalities, part 1: Existence theory for the elliptic case. J. Optim. Theory Appl. **69**, 351–371 (1991)
23. Liu, W.B., Rubio, J.E.: Optimal shape design for systems governed by variational inequalities, part 2: Existence theory for the evolutionary case. J. Optim. Theory Appl. **69**, 373–396 (1991)
24. Michor, P.W., Mumford, D.: An overview of the Riemannian metrics on spaces of curves using the Hamiltonian approach. Appl. Comput. Harmon. Anal. **23**, 74–113 (2007)
25. Mohammadi, B., Pironneau, O.: Applied Shape Optimization for Fluids. Numerical Mathematics and Scientific Computation. Clarendon Press, Oxford (2001)
26. Myślinśki, A.M.: Domain optimization for unilateral problems by an embedding domain method. In: Cagnol, J., Polis, M.P., Zolésio, J. (eds.) Shape Optimization and Optimal Design. Lecture Notes in Pure and Applied Mathematics, vol. 216, pp. 355–370. Marcel Dekker, New York (2001)

27. Myśliński, A.M.: Level set approach for shape optimization of contact problems. In: Neittaanmäki, P., Rossi, T., Majava, K., Pironneau, O., Lasiecka, I. (eds.) European Congress on Computational Methods. Applied Sciences and Engineering ECCOMAS 2004 (2004)
28. Myśliński, A.: Level set method for shape and topology optimization of contact problems. In: Korytowski, A., et al. (eds.) System Modelling and Optimization. IFIP Advances in Information and Communication Technology, vol. 312, pp. 397–410. Springer, Berlin (2007)
29. Nägel, A., Schulz, V., Siebenborn, M., Wittum, G.: Scalable shape optimization methods for structured inverse modeling in 3D diffusive processes. Comput. Visual. Sci. **17**, 79–88 (2015)
30. Novotny, A.A., Sokołowski, J.: Topological Derivatives in Shape Optimization. Springer, Berlin (2013)
31. Paganini, A.: Approximative shape gradients for interface problems. Tech Rep. 2014-12. ETH Zürich, Seminar for Applied Mathematics (2014)
32. Ring, W., Wirth, B.: Optimization methods on Riemannian manifolds and their application to shape space. SIAM J. Optim. **22**, 596–627 (2012)
33. Schmidt, S.: Weak and strong form shape Hessians and their automatic generation. SIAM J. Sci. Comput. **40**, C210–C233 (2018)
34. Schmidt, S., Ilic, C., Schulz, V., Gauger, N.: Three-dimensional large-scale aerodynamic shape optimization based on the shape calculus. AIAA J. **51**, 2615–2627 (2013)
35. Schulz, V.: A Riemannian view on shape optimization. Found. Comput. Math. **14**, 483–501 (2014)
36. Schulz, V., Siebenborn, M.: Computational comparison of surface metrics for PDE constrained shape optimization. Comput. Methods Appl. Math. **16**, 485–496 (2016)
37. Schulz, V., Siebenborn, M., Welker, K.: Structured inverse modeling in parabolic diffusion problems. SIAM J. Control Optim. **53**, 3319–3338 (2015)
38. Schulz, V., Siebenborn, M., Welker, K.: Towards a Lagrange–Newton approach for PDE constrained shape optimization. In: Pratelli, A., Leugering, G. (eds.) New Trends in Shape Optimization. International Series of Numerical Mathematics, vol. 166, pp. 229–249. Springer, Switzerland (2015)
39. Schulz, V., Siebenborn, M., Welker, K.: A novel Steklov-Poincarétype metric for efficient PDE constrained optimization in shape spaces. SIAM J. Optim. **26**, 2800–2819 (2016)
40. Siebenborn, M., Welker, K.: Algorithmic aspects of multigrid methods for optimization in shape spaces. SIAM J. Sci. Comput. **39**, B1156–B1177 (2017)
41. Sokolowski, J., Zolesio, J.-P.: Introduction to Shape Optimization. Springer Series in Computational Mathematics, vol. 16. Springer, Berlin (1992)
42. Toffel, R.: Structural Optimization of Coupled Problems. Ph.D. thesis, Universität Trier (2013). http://ubt.opus.hbz-nrw.de/volltexte/2014/838/
43. Udawalpola, R., Berggren, M.: Optimization of an acoustic horn with respect to efficiency and directivity. Int. J. Numer. Methods Eng. **73**, 1571–1606 (2007)
44. Welker, K.: Efficient PDE Constrained Shape Optimization in Shape Spaces. Ph.D. thesis, Universität Trier (2016). http://ubt.opus.hbz-nrw.de/volltexte/2017/1024/
45. Welker, K.: Suitable spaces for shape optimization. arXiv:1702.07579 (2017)